J. Fluid Mech. (2008), *vol.* 599, *pp.* 241–268.
doi:10.1017/S0022112008000153 Printed in the United Kingdom

The turbulent equilibration of an unstable baroclinic jet

J. G. ESLER

Department of Mathematics, University College London, 25 Gower Street,
London WC1E 6BT, UK
gavin@math.ucl.ac.uk

(Received 18 April 2007 and in revised form 30 November 2007)

The evolution of an unstable baroclinic jet, subject to a small perturbation, is examined numerically in a quasi-geostrophic two-layer β-channel model. After a period of initial wave growth, wave breaking leads to turbulence within each layer, and to the eventual equilibration of the flow. The equilibrated flow must satisfy certain dynamical constraints: total momentum is conserved, the total energy is bounded and the flow must be realizable via some area-preserving (diffusive) rearrangement of the initial potential vorticity field in each layer. A theory is introduced that predicts the equilibrated flow in terms of the initial flow parameters. The idea is that the equilibrated state minimizes available potential energy, subject to the constraints on total momentum and total energy, and the further 'kinematic' constraint that the potential vorticity changes through a process of complete homogenization within well-delineated regions in each layer. Within a large region of parameter space, the theory accurately predicts the cross-channel structure and strength of the equilibrated jet, the regions where potential vorticity mixing takes place, and total eddy mass (temperature) fluxes. Results are compared with predictions from a maximum-entropy theory that allows for more general rearrangements of the initial potential vorticity field, subject to the known dynamical constraints. The maximum-entropy theory predicts that significantly more available potential energy is released than is observed in the simulations, and that an unphysical 'exchange' of bands of fluid will occur across the channel in the lower layer. The kinematic constraint of piecewise potential vorticity homogenization is therefore important in limiting the 'efficiency' of release of available potential energy in unstable baroclinic flows. For a typical initial flow, it is demonstrated that if the dynamical constraints alone are considered, then over twice as much potential energy is available for release compared to that actually released in the simulations.

1. Introduction

Arguably the central theoretical challenge in both atmospheric dynamics and physical oceanography is to obtain a systematic quantitative understanding of the interactions between large-scale mean flows and eddy activity. Such understanding may serve as the basis for accurate parameterization of mesoscale eddies in large-scale ocean climate models, and thus lead to a large increase in the capacity of the models to simulate the ocean circulation on decadal and centennial time scales at relatively low computational cost. Idealized fluid dynamical models, with highly simplified 'physics' (meaning parameterized physical processes), are usually used as

testbeds for hypotheses regarding the dynamical processes governing eddy/mean-flow interaction. Typically, these models are designed to simulate the circulation obtained when the models are initialized with, or forced towards, a mean state that is unstable to baroclinic instability. The behaviour of such models in atmospheric and oceanic contexts have been discussed in several recent reviews (Held 2007; Zurita-Gotor & Lindzen 2007; McWilliams 2006, Chap. 5).

The current study will examine the behaviour of arguably the most established testbed, the quasi-geostrophic two-layer channel model (Phillips 1951). The two-layer model remains widely studied as it is considered to be the simplest model to capture most of the essential elements of the extratropical tropospheric circulation (e.g. Held 2005; Zurita-Gotor 2007), as well as ocean currents such as the Gulf Stream and the Antarctic circumpolar current (e.g. Arbic & Flierl 2004). The aim of this work is to take a step back from the challenging, although much studied, problem of formulating a predictive theory for the forced–dissipative equilibria, or 'two-layer climates' that occur in the model (see e.g. Held & Larichev 1996; Pavan & Held 1996; Zurita-Gotor 2007). Instead, an idealized problem of quasi-geostrophic turbulence will be addressed: how do eddies act to equilibrate an initially unstable baroclinic jet in the unforced problem? A complete understanding of the unforced problem, which might be aptly described as the 'baroclinic lifecycle problem' (see e.g. Feldstein & Held 1989; Thorncroft, Hoskins & McIntyre 1993) is of interest for the following three reasons:

(i) A complete understanding of the unforced problem might be seen as a necessary precondition for a complete theory (generalizing the 'baroclinic adjustment' theories described below) of the forced–dissipative problem. Such a theory would represent a breakthrough in our fundamental understanding of the extratropical atmospheric circulation (e.g. Zurita-Gotor & Lindzen 2007).

(ii) Understanding the baroclinic wave lifecycle problem is also of importance as numerical simulations of the lifecycles serve as important paradigms for the observed behaviours of extratropical cyclones (e.g. Thorncroft *et al.* 1993). At present, changes in the zonal mean (eastwards) zonal flow during lifecycles are not fully understood.

(iii) Finally, the baroclinic lifecycle problem is of interest from the point of view of theoretical investigations of the behaviour of rotating fluids at very high Reynolds number, in that it is typical of a class of idealized flows that may serve as a test for various predictive theories based on statistical fluid mechanics (see e.g. Majda & Wang 2006).

For these reasons, the baroclinic lifecycle problem can be regarded as a fundamental model problem in geophysical fluid dynamics. The quasi-geostrophic two-layer model is adopted here as a simple model of baroclinic lifecycles and it should be noted that a significant effect in flows with finite Rossby number, the adjustment of static stability (Gutowksi 1985; Schneider & Walker 2006), is excluded under the quasi-geostrophic approximation. The aim here is to present a predictive theory for the changes to the mean flow that occur as the initially unstable two-layer jet undergoes turbulent equilibration.

Previous studies of the equilibration of an unstable baroclinic jet in the two-layer model (Feldstein & Held 1989; Nakamura 1999) have focused on the properties of the most unstable linear normal mode. These studies have established that if critical levels of this mode exist to the flanks of the jet in the upper layer then the equilibration of the jet is highly asymmetric in the vertical. Mixing of potential vorticity (PV) is observed to occur across the centre of the channel in the lower layer and to the flanks of the jet in the upper layer, with a corresponding *increase* in the strength of

the jet itself. Near the jet core, therefore, momentum fluxes are upgradient; a feature that has been long observed in the extratropical atmosphere. Upgradient momentum fluxes appeared paradoxical to early researchers, because if a simple turbulent closure based on the Reynolds' stress is employed, then it appears that eddy activity acts as a 'negative viscosity' (Starr 1968). Modern theories of wave–mean interaction (see e.g. the review by Dritschel & McIntyre 2008) provide an explanation: upgradient momentum fluxes are dynamically consistent with the observed downgradient mixing of PV, and it is PV (not momentum) that is considered to be the relevant quantity for eddy flux closure theories (e.g. Wardle & Marshall 2000) since it is conserved following fluid parcels in adiabatic, frictionless flow.

Notwithstanding the above theoretical developments, both eddy flux closures based on PV flux–gradient relationships (e.g. Pavan & Held 1996) and turbulent scaling theories (e.g. Held & Larichev 1996; Lapeyre & Held 2003) have had limited success in characterizing the behaviour of simulated forced–dissipative flows. These approaches do not capture the highly inhomogeneous nature of simulated PV fluxes; for example, why does turbulent mixing of PV in two-layer flows occur at the jet flanks in the upper layer and across the centre of the channel in the lower layer? An alternative approach, relevant to both forced-dissipative and initial value problems, is the 'baroclinic adjustment' theory of Stone (1978). In Stone's 'local adjustment' approach, eddies are assumed act to stabilize the flow by reducing the local vertical wind shear to some critical value, thereby stabilizing the mean flow. However, local baroclinic adjustment theory does not allow for upgradient momentum fluxes, nor can it account for the sensitivity of unstable baroclinic flows to the horizontal structure of the flow (James 1987). These limitations have been recognized by Nakamura (1993, 1999), who has presented useful insights into how a generalized adjustment theory might work, from the perspective of linear wave dynamics and PV mixing.

In this work it will be demonstrated that it is the *global* constraints on flow development that are the key to correctly predicting the outcome of numerical simulations. Combining the global constraints with a minimization principle for the available potential energy is shown to lead to a generalized baroclinic adjustment theory that quantitatively accounts for upgradient momentum fluxes. Notably, linear wave theory is not explicitly invoked by this theory at all.

In § 2 the model and its numerical implementation are introduced, the known physical laws that constrain the fluid motion are stated, and the evolution of a typical flow is described. In § 3 a theory to predict the final equilibrated flow state is formulated, and the predictions of this theory are compared in detail with the results of numerical simulations. In § 4 the numerical results are further compared with predictions from a 'maximum-entropy' theory following the statistical mechanics approach of Miller (1990), Robert (1991) and Robert & Sommeria (1991). In § 5 a new technique is described that can be used to explore the manifold of permissible flows under the dynamical constraints, and in principle to find extrema of any quantity on this manifold. Low-potential-energy states are calculated and compared with the predictions of § 3. Finally conclusions are presented in § 6.

2. Model and numerical experiments

2.1. *Quasi-geostrophic two-layer channel model*

The quasi-geostrophic two-layer model (Phillips 1951) describes flow in a re-circulating channel that is periodic in the x-direction (longitude), with length L_x^*, and has sidewalls at fixed latitudes $y = \pm L_y^*/2$. The channel, shown schematically in figure 1(a),

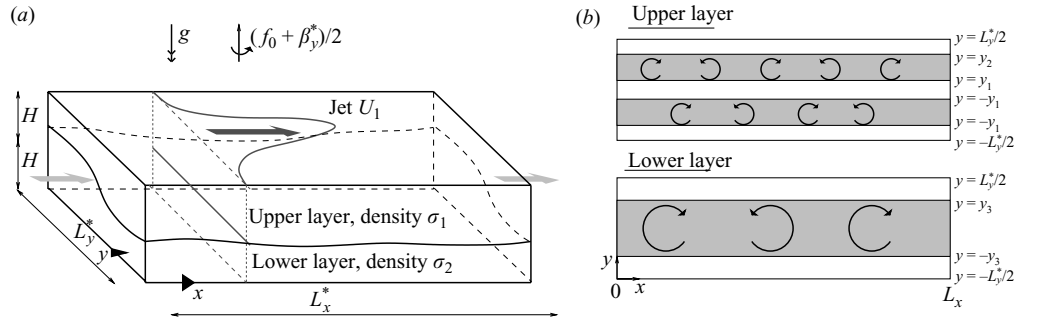

FIGURE 1. (*a*) Schematic picture of the Phillips' quasi-geostrophic two-layer model, initialized with an upper layer jet. (*b*) Schematic illustrating those regions where turbulent mixing develops during the flow evolution in the upper and lower layers, and defining the latitudes y_1, y_2 and y_3.

represents a latitude band in the midlatitudes of a rotating planet, and under the β-plane approximation (e.g. Pedlosky 1987) can be assumed to have rectilinear geometry and to rotate differentially at rate $f/2$, where $f = f_0 + \beta^* y$. The upper and lower fluid layers each have undisturbed depth H, evolve under gravity g, and have density ϱ_1 and ϱ_2 ($> \varrho_1$) respectively. It is taken that $2(\varrho_2 - \varrho_1)/(\varrho_1 + \varrho_2) \ll 1$, in order that the Boussinesq approximation may be used, i.e. a 'reduced gravity' $g' = 2g(\varrho_2 - \varrho_1)/(\varrho_1 + \varrho_2)$ acts on the interface between the layers and the pressure gradient at the upper-layer free surface is identical to that in the presence of a rigid lid. The evolution of a initially unstable upper-layer jet, flowing in the positive x-direction (eastward) with maximum velocity U is to be considered. The flow is viscous with kinematic viscosity ν^*. Interfacial and bottom friction are neglected. Following Pedlosky (1987) and Lee & Held (1993) the equations of motion for a rotating two-layer shallow fluid can be non-dimensionalized, taking horizontal length scales equal to the internal Rossby radius $L_D = \sqrt{g'H/2f_0^2}$, vertical length scale H, time scale L_D/U, and horizontal and vertical velocity scales U, UH/L_D. If the Rossby/Froude number satisfies $\epsilon = U/f_0 L_D (= \sqrt{2}U/\sqrt{g'H}) \ll 1$, then geostrophic flow is found to hold at leading order. A geostrophic streamfunction ψ_i can then be defined in each layer ($i = 1, 2$) from which the leading-order velocity can be obtained via $\boldsymbol{u}_i = -\nabla \times \psi_i \boldsymbol{k}$. Proceeding to the next order in ϵ, the equations of motion are (Pedlosky 1987)

$$\frac{\mathrm{D}_i q_i}{\mathrm{D}t} = \kappa \nabla^4 \psi_i, \quad i = 1, 2, \tag{2.1}$$

$$q_i \equiv \beta y + \nabla^2 \psi_i + (-1)^i \left(\frac{\psi_1 - \psi_2}{2} \right), \tag{2.2}$$

$$\frac{\mathrm{D}_i}{\mathrm{D}t} \equiv \partial_t - \psi_{iy} \partial_x + \psi_{ix} \partial_y. \tag{2.3}$$

Here q_i is the quasi-geostrophic potential vorticity in layer $i = 1, 2$. Assuming no zonal flow on the sidewalls, the streamfunction ψ_i is subject to boundary conditions

$$\psi_{ix} = 0, \quad \overline{\psi}_{iy} = 0, \quad \text{on} \quad y = \pm \frac{L_y}{2}, \quad i = 1, 2, \tag{2.4}$$

where the overbar denotes an x-average (zonal average), and $L_x = L^*_x/L_D$, $L_y = L^*_y/L_D$ are the non-dimensional channel dimensions.

The non-dimensional parameters in (2.1)–(2.3) are

$$\beta = \frac{\beta^* L_D^2}{U}, \quad \kappa = \frac{\nu^*}{U L_D}.$$

The inverse criticality β is a measure of the degree of instability of the jet, while κ is an inverse (Rossby-)Reynolds number and measures the importance of viscous effects. Following Pavan & Held (1996), the initial jet is chosen to have latitudinal profile

$$U_1 = -\psi_{1y} = \mathrm{sech}^2\left(\frac{y}{\sigma}\right), \quad U_2 = -\psi_{2y} = 0. \tag{2.5}$$

The parameter σ, the jet half-width scaled by the Rossby radius (L_D), is chosen to be much less than the non-dimensional channel width L_y in order to minimize the influence of the sidewalls on the flow evolution. Here attention is restricted to $\sigma \lesssim 3$ in order that the flow on the sidewalls can be neglected. If a uniform flow is chosen as the initial condition as opposed to an isolated jet, the sidewalls would necessarily control the nonlinear stages of the flow evolution (see Warn & Gauthier 1989).

Although the qualitative behaviour of typical two-layer model flows resembles that observed in the atmosphere and ocean, there are pitfalls associated with making exact quantitative comparisons and deriving appropriate parameter values directly from observations (e.g. Held 2007). Nevertheless, taking $L_D = 800\,\mathrm{km}$, $\beta^* = 1.6 \times 10^{-11}\,\mathrm{m^{-1}\,s^{-1}}$ and $U = 40\,\mathrm{m\,s^{-1}}$, as can be argued to be appropriate for the observed midlatitude tropospheric jets, results in a value $\beta \approx 0.25$. A non-dimensional jet half-width of $\sigma = 2$ (units L_D) is a good fit to observations. Hence parameter values $(\beta, \sigma) = (0.25, 2)$ are used in the reference simulation described below. For the ocean the internal Rossby radius is typically $L_D = 50\,\mathrm{km}$ (following Arbic & Flierl 2004), therefore the reference simulation is relevant for midlatitude currents with $U \approx 0.1\,\mathrm{m\,s^{-1}}$. In both atmosphere and ocean, the relevant value of κ (approximately 5×10^{-13} and 2×10^{-10} respectively if molecular kinematic viscosities are used) is much lower than can be attained in the numerical simulations. However, convergence of results with respect to κ will be demonstrated below.

To initialize the numerical simulations described below, a perturbation with the form

$$\tilde{q}_1(x, y) = \varepsilon \left(x - \tfrac{1}{2}L_x\right) \exp[-((x - L_x/2)^2 + y^2)/R^2],$$

is added to the upper-layer PV field. In all simulations described below $\varepsilon = 0.04$ and $R = 2$. Note that the initial perturbation $\tilde{q}_1$ is localized in physical space (as opposed to being a periodic wave) in order that the fastest growing disturbances may naturally emerge during the subsequent evolution. This approach avoids biasing the results by removing any artificial symmetry associated with a particular zonal wavenumber.

2.2. *Numerical implementation*

The numerical model used to obtain solutions of (2.1)–(2.4) is adapted from that of Esler & Haynes (1999). A standard pseudo-spectral representation is used in the x-direction and a grid-point representation in the y-direction. At fixed numerical resolution, converged solutions of (2.1) can be obtained only for values of κ greater than some threshold value. Diffusivity greater than the threshold value is necessary to dissipate sufficient enstrophy at small scales, thereby preventing the forward cascade of enstrophy in wavenumber space resulting in a spurious build-up of enstrophy at the model grid scale. One property of a converged solution, therefore, is that the enstrophy spectrum at large wavenumbers is monotonically decreasing.

Numerical resolution	Fourier modes (x)	Grid points (y)	δt (f_0^{-1})	κ
High (HR)	1024	641	0.0005	2×10^{-4}
Medium (MR)	512	321	0.001	7.5×10^{-4}
Low (LR)	256	161	0.002	2.5×10^{-3}

TABLE 1. Values of the numerical parameters used in the simulations.

Table 1 shows the range of numerical resolutions used in the calculations, the value of κ used in conjunction with each resolution, together with the model time-step δt used in each case. Independence of model time-step, within limits determined by the Courant–Friedrichs–Lewy criterion, has been verified directly. Independence of the model grid is verified by repeating the high-resolution calculation (HR) with $\kappa = 7.5 \times 10^{-4}$, i.e. the value associated with the medium-resolution (MR) simulations. Mean field quantities and energy and enstrophy spectra are found to be unchanged from the MR results.

As will be demonstrated explicitly below, results derived from integrations for a fixed time period are found to be largely independent of κ, provided κ is sufficiently small. The channel length and width are set to $L_x = 20\pi$ and $L_y = 5\pi$ Rossby radii (L_D) respectively, values which are appropriate if the channel corresponds to the extratropical troposphere. With L_x and L_y fixed, each integration is defined by the values of the inverse criticality and non-dimensional jet width (β, σ). The current investigation is restricted to the region of parameter space $\beta \in [0.2, 0.35]$, $\sigma \in [1.5, 3]$.

Figure 2 shows this region of parameter space, together with the boundaries that demarcate transitions to different behaviour. For $\beta \geqslant 0.5$ the Charney–Stern–Pedlosky criterion for instability (e.g. Pedlosky 1987), which states that a necessary condition for instability is that the potential vorticity gradient must change sign somewhere in the channel in either layer (a generalized Rayleigh inflection point criterion), is not satisfied and the flow is stable. For $0.2 < \beta < 0.5$ and $\sigma \in [2, 3]$ there is a single region of negative PV gradient in the centre of the lower layer, consistent with baroclinic instability. For $\sigma \lesssim 1.5$, however, further regions of negative PV gradient appear at the flanks of the jet (either in the upper-layer PV or in the vertically integrated PV). The presence of these further regions of negative PV gradient indicate that a more complex (mixed baroclinic–barotropic) instability will emerge, and therefore that the instability will have a different character at small values of σ. At large σ other processes become important. If the jet width is much greater than the Rhines scale (Rhines 1975) (under the assumption that the turbulent eddy velocity scale in the problem scales with the initial velocity this corresponds to $\sigma \gg \beta^{-1/2}$) multiple jet formation will occur (see also Pavan & Held 1996). For this reason, and because it is desirable that the jet is located away from the channel walls, attention is restricted to $\sigma \leqslant 3$. Finally, as β decreases below approximately 0.2 a qualitative transition in behaviour occurs for two reasons, as will be discussed further below. First the active regions of the developing flow reach the channel walls, and consequently the location of the walls themselves becomes important. Secondly, and intriguingly, a qualitative change in the behaviour of the upper-layer jet is evident as the upper-layer mixing regions extend to the centre of the channel.

The symbols on figure 2 mark the parameter settings for the numerical simulations to be discussed below. In most cases medium resolution (MR, see table 1) is used, except for the reference run $(\beta, \sigma) = (0.25, 2)$ described below, the $\beta = 0.2$ set of simulations, and the $\sigma = 1.5$ set of simulations, for which high resolution (HR) is also

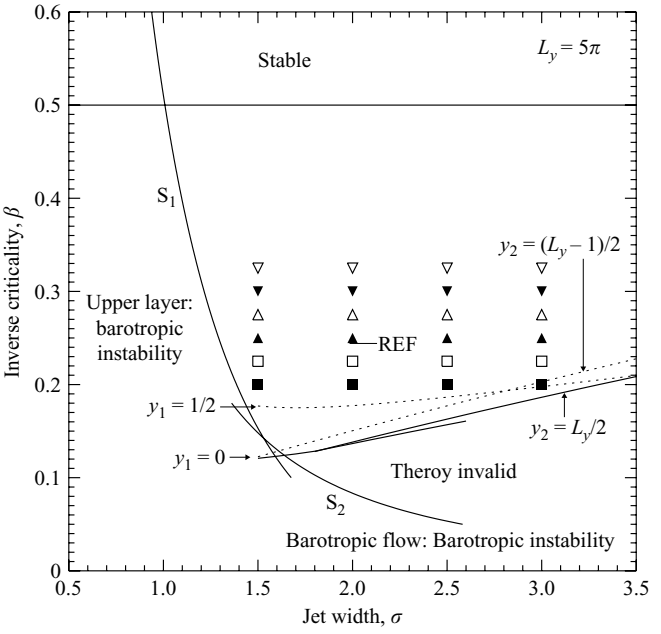

FIGURE 2. Regime diagram in inverse criticality/jet width (β, σ) parameter space, illustrating the region of parameter space under investigation. For $\beta > 0.5$ the flow does not meet the Charney–Stern–Pedlosky necessary condition for baroclinic instability. To the left of curve S_1, PV gradient reversals occur in the jet flanks in the upper layer, and to the left of curve S_2 PV gradient reversals occur in the layerwise mean PV $Q_1 + Q_2$. Any instability will therefore have a mixed barotropic–baroclinic character to the left of these curves, which from (3.2) can be shown to have equations $\beta = (2/3\sigma^2)(1 - \sigma^2/8)^2$ and $\beta = 1/3\sigma^2$ respectively. The remaining curves demarcate the regions where the theory of § 3 might be expected to be valid (see text). Points mark the location of numerical experiments, and are labelled according to the value of β.

used as a check on results. There are no significant differences to report between the MR and HR results.

2.3. *Physical constraints*

For $\beta < 0.5$ and small κ, the flow is unstable and wave growth followed by layerwise turbulence ensues. The evolving flow, however, is subject to a number of dynamical constraints that must be accounted for in any theory that seeks to predict the final equilibrium state.

First, total momentum M is conserved between the two layers:

$$\frac{\mathrm{d}M}{\mathrm{d}t} = \frac{\mathrm{d}}{\mathrm{d}t}\int_D u_1 + u_2 \ \mathrm{d}^2\boldsymbol{x} = \frac{\mathrm{d}}{\mathrm{d}t}\int_D y(q_1 + q_2)\,\mathrm{d}^2\boldsymbol{x} = 0, \tag{2.6}$$

where the domain D is the channel $\{x \in [0, L_x], y \in [-L_y/2, L_y/2]\}$. Hence $M = M_0 = 4L_x\sigma \tanh(L_y/2\sigma)$, the initial total momentum of the flow throughout the flow evolution. The second constraint is on the total energy E, which satisfies

$$\begin{aligned}\frac{\mathrm{d}E}{\mathrm{d}t} &= \frac{\mathrm{d}}{\mathrm{d}t}\,\frac{1}{2}\int_D |\nabla\psi_1|^2 + |\nabla\psi_2|^2 + \frac{(\psi_2 - \psi_1)^2}{2}\ \mathrm{d}^2\boldsymbol{x}, \\ &= -\frac{\mathrm{d}}{\mathrm{d}t}\frac{1}{2}\int_D \psi_1 q_1 + \psi_2 q_2\ \mathrm{d}^2\boldsymbol{x} = -\kappa\int_D |\nabla^2\psi_1|^2 + |\nabla^2\psi_2|^2\ \mathrm{d}^2\boldsymbol{x}.\end{aligned} \tag{2.7}$$

As the energy sink term is negative definite, the energy satisfies $E \leqslant E_0$, where E_0 is the initial energy.

Finally, an important set of constraints is due to the fluid parcelwise conservation of PV (2.1). Any functional of the PV of the form

$$\mathscr{C}[q_i] = \int_D C_1(q_1) + C_2(q_2)\,\mathrm{d}^2\boldsymbol{x}, \tag{2.8}$$

is conserved in inviscid flow ($\kappa = 0$) for arbitrary functions C_1 and C_2. For flows with κ small but non-zero such functionals might no longer be conserved, but are nevertheless associated with important constraints on the flow evolution that must be accounted for. One method of imposing these constraints is to require that the evolving PV satisfies $q_i \in \mathscr{R}(Q_i)$, where $\mathscr{R}(Q_i)$ is the set of 'conservative rearrangements' of the initial PV field Q_i. The concept of 'conservative rearrangement' will be defined rigorously below, but the basic idea is that it must be possible to construct such a PV distribution by a parcelwise rearrangement of the initial PV field, followed by the application of a smoothing operation that is consistent with the presence of diffusion.

It is noteworthy that none of the constraints (2.6)–(2.8) can be applied directly to obtain bounds on the wave energy, as all involve contributions from the mean flow. However, linear combinations of (2.6)–(2.8), with judicious choice of the functions $C_1(q_1)$ and $C_2(q_2)$ can be used to obtain rigorous bounds on dynamical quantities which involve terms that are quadratic (or higher) in disturbance amplitude, with disturbances being defined relative to some stable 'background' flow. These quantities are termed 'wave pseudo-momentum' (derived from (2.6) and (2.8) (see Shepherd 1988)), and 'wave pseudo-energy' (derived from (2.7) and (2.8) (e.g. McIntyre & Shepherd 1987)). Note that no new information is contained in the pseudo-momentum and pseudo-energy, i.e. any flow constrained by (2.6)–(2.8) will automatically satisfy all relevant pseudo-momentum and pseudo-energy inequalities.

2.4. *Evolution and energetics of a typical flow*

Figure 3 shows snapshots of the upper- and lower-layer potential vorticity (PV) fields during the equilibration of the reference flow, with $(\beta, \sigma) = (0.25, 2)$, at low κ (2×10^{-4}, see table 1). At early times linear dynamics applies and the initial disturbance grows exponentially according to its projection onto the normal modes of the initial state. As the flow develops, nonlinear saturation of the growing waves is observed first in the lower layer, where PV contours wrap up in the centre of the channel, as can be seen in the $t = 100 f_0^{-1}$ lower-layer panel (*b*). In the upper layer at $t = 100 f_0^{-1}$, meanwhile, PV stirring is seen to occur to the flanks of the jet in the centre of the channel. The jet itself is seen to support large-amplitude waves. As the flow develops further, these waves begin to decay. The wave decay is an almost entirely inviscid process, as can be seen from the near conservation of total energy, plotted in figure 4 (solid TE curve). Rather, the wave or eddy energy (solid EKE+EPE curve in figure 4) extracted from the mean flow during the linear growth stage is returned to the mean flow via inviscid turbulent processes. In the atmospheric literature, the above process is often referred to as a 'baroclinic growth-barotropic decay' cycle (Simmons & Hoskins 1978; Thorncroft *et al.* 1993).

As is clear from figure 4, by the end of the cycle at $t = 250 f_0^{-1}$, the net effect of the growth and decay of the eddies is the conversion of zonal (east–west) mean potential energy (ZPE) to zonal mean kinetic energy (ZKE). This corresponds to an acceleration of the jet in each layer, relative to its initial state. Snapshots of the PV at time $t = 250 f_0^{-1}$ (figure 3) reveal that the waves have decayed almost completely in

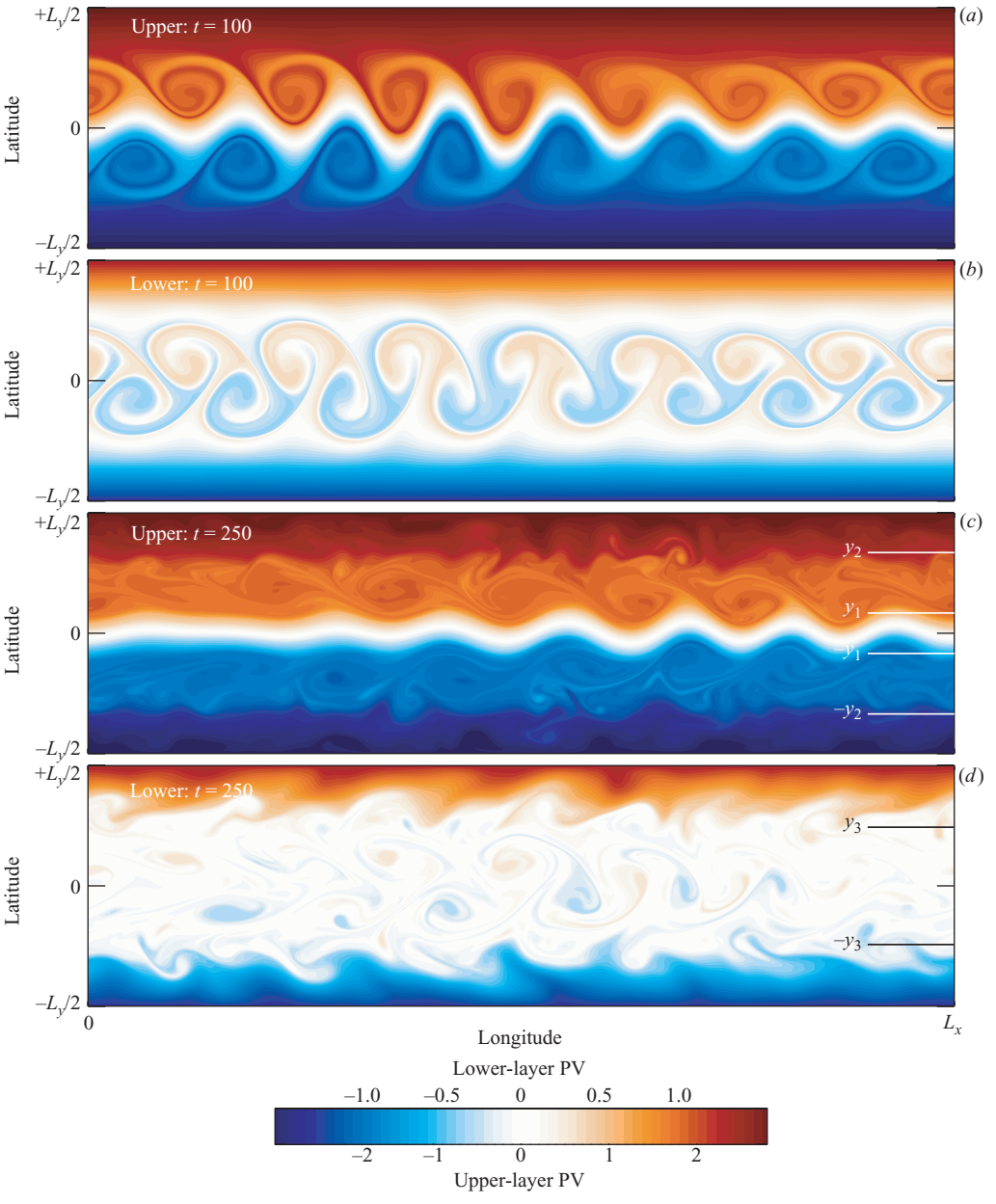

FIGURE 3. (a, b) Upper-layer PV q_1 and lower-layer PV q_2 snapshots at $t = 100 f_0^{-1}$ from the reference experiment $(\beta, \sigma) = (0.25, 2)$, at low κ (2×10^{-4}). (c, d) As for (a, b) but for $t = 250 f_0^{-1}$.

each layer, leaving distinct regions of relatively weak turbulence in the centre of the lower layer and to the flanks of the jet in the upper layer. Outside the turbulent regions the flow is laminar and mostly zonal, perturbed only by relatively small-amplitude waves which have little associated energy.

By $t = 250 f_0^{-1}$ the rate of change of the zonal mean flow in each layer has slowed dramatically, as the jet is now evolving only under the action of the very weak diffusion. It is this near-zonal, near-steady state that we aim to predict below.

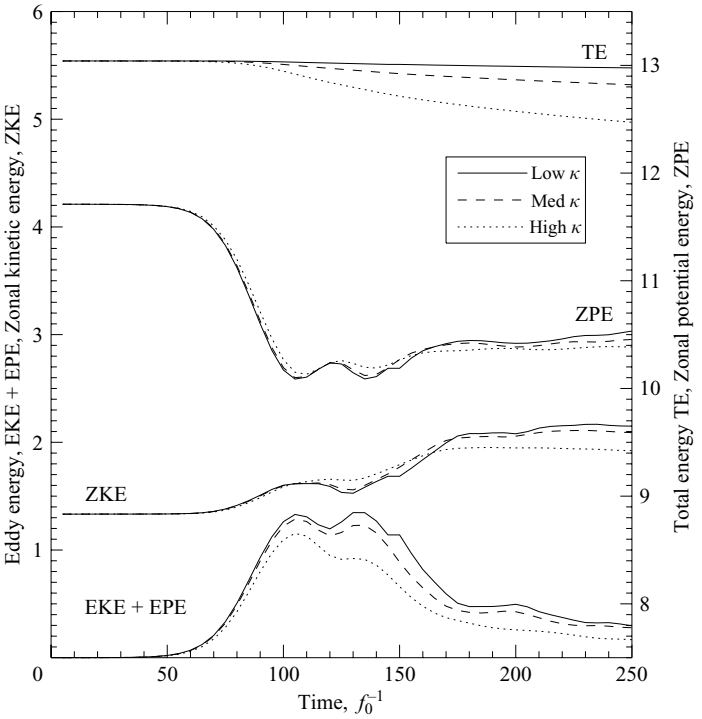

FIGURE 4. Time evolution of non-dimensional energetic quantities for the reference experiment $(\beta, \sigma) = (0.25, 2)$ repeated for low (2×10^{-4}, solid curves), medium (7.5×10^{-4}, dashed curves) and high (3×10^{-3}, dotted curves) values of κ. Quantities plotted are (left axis) total eddy energy (EKE + EPE), zonal mean kinetic energy (ZKE) and (right axis) zonal mean potential energy (ZPE) and total energy (TE).

3. Theory for baroclinic equilibration via PV homogenization

3.1. *Statement of the 'equilibration via PV homogenization' hypothesis*

The qualitative features of the evolution of the energetics and PV distribution described for the simulation above are typical of those observed throughout the range of jet parameters (β, σ) under consideration. On the basis that baroclinic instability is driven primarily by the release of available potential energy, and that the energy released is almost entirely returned to zonal mean kinetic energy, the following hypothesis for baroclinic equilibration is proposed:

Equilibration via PV Homogenization (EPVH) hypothesis: The active eddy field forces the mean flow towards a final, near-steady, equilibrated state that has the minimum possible available potential energy, subject to the constraints of conservation of total zonal momentum and total zonal energy, and the additional kinematic constraint that all mixing processes result in potential vorticity homogenization within well-delineated regions.

The assumptions underpinning the EPVH hypothesis can be described as follows:

(*a*) A negligible amount of total energy is lost to dissipation.

(*b*) All but a negligible proportion of the total energy of the flow is returned to the zonal mean. Equivalently, the baroclinic growth–barotropic decay cycle described above is assumed to proceed to completion.

(*c*) All of the mixing which takes place during the equilibration results in PV homogenization within distinct regions of the channel that are bounded in latitude.

(*d*) The flow acts to minimize the total available potential energy subject to the dynamical constraints, interpreted following (*a–c*).

The results shown in figures 3 and 4 lend strong support to the proposition that assumptions (*a–c*) hold to a good approximation in the reference $(\beta, \sigma) = (0.25, 2)$ simulation described above, and similar results are found for the remaining simulations. In simulations with low β, assumption (*b*) is found to break down whenever the mixing regions in either layer are found to extend to the sidewalls. A similar influence of sidewall behaviour on the qualitative development of baroclinic lifecycles has been found by Mak (2000). Assumption (*d*) is necessary to close the system, and is motivated by the idea that baroclinic instability is driven by a release of potential energy. The assumption is simply that the release of available potential energy, meaning here that part of the potential energy V that is available for release after accounting for all of the dynamical constraints, continues until it is exhausted. By definition a flow without available potential energy cannot be unstable to baroclinic instability. The above formulation of the EPVH theory is directly applicable to baroclinic lifecycle flows such as those described in § 2. It is straightforward in principle to generalize the theory to more complicated lifecycles with asymmetric initial jets and/or more vertical structure. The question of whether the same principles can be adapted to predict the climates of forced–dissipative flows is discussed in § 6.

The numerical integrations indicate that those regions where PV homogenization actually occurs are the three highlighted in figure 1(*b*). Two of these regions are located at the flanks of the upper-layer jet, between latitudes y_1 and y_2, and $-y_2$ and $-y_1$ respectively, where $0 < y_1 < y_2 \leqslant L_y/2$. The third region spans the centre of the channel in the lower layer between $-y_3$ and y_3 $(0 < y_3 \leqslant L_y/2)$. The aim of the EPVH theory then, as formulated below, is to predict the values of y_1, y_2 and y_3 using only the flow parameters, together with the details of the initial jet structure. The predicted structure of the jet in each layer, as well as the net mass flux in the channel due to the instability, can then be calculated from the values of y_1, y_2 and y_3.

3.2. *Formulation of the EPVH theory*

If complete PV homogenization takes place in the regions shown in figure 1(*b*), the final PV distribution $q_i(y)$ can be expressed straightforwardly in terms of the initial PV $Q_i(y)$, as

$$q_1(y) = \begin{cases} Q_1(y), & y_2 < y < \frac{1}{2}L_y \\ Q_m, & y_1 < y < y_2 \\ Q_1(y), & -y_1 < y < y_1 \\ -Q_m, & -y_2 < y < -y_1 \\ Q_1(y), & -\frac{1}{2}L_y < y < -y_2, \end{cases} \qquad q_2 = \begin{cases} Q_2(y), & y_3 < y < \frac{1}{2}L_y \\ 0, & -y_3 < y < y_3 \\ Q_2(y), & -\frac{1}{2}L_y < y < -y_3. \end{cases} \tag{3.1}$$

where the initial PV can be calculated from equations (2.5) and (2.2) to be

$$Q_1(y) = \beta y + \tanh\left(\frac{y}{\sigma}\right)\left[\frac{2}{\sigma}\operatorname{sech}^2\left(\frac{y}{\sigma}\right) + \frac{\sigma}{2}\right], \quad Q_2(y) = \beta y - \frac{\sigma}{2}\tanh\left(\frac{y}{\sigma}\right), \tag{3.2}$$

and

$$Q_m = \frac{1}{y_2 - y_1} \int_{y_1}^{y_2} Q_1(y)\,\mathrm{d}y.$$

Given $\{y_1, y_2, y_3\}$, predictions for the final streamfunction ψ_i, and the final zonal velocity $u_i = -\psi_{iy}$ can be obtained straightforwardly from q_i using (2.2) and (2.4).

The aim of the EPVH theory is, given values of (β, σ), to predict values of $\{y_1, y_2, y_3\}$ that minimize the potential energy V stored in the sloping interface,

$$V = \int_D \frac{(\psi_2 - \psi_1)^2}{4}\,\mathrm{d}^2\boldsymbol{x} \tag{3.3}$$

subject to the constraints described above. Under assumptions (a, b) this is equivalent to minimizing the zonal mean potential energy $\overline{V}$. The dynamical constraint that the final PV distribution $q_i \in \mathscr{R}(Q_i)$, i.e. q_i is in the set of conservative rearrangements of the initial PV field Q_i (formally defined in §4 below), is enforced automatically by our assumption of PV homogenization within the regions shown in figure 1(*b*). This leaves the constraints on zonal mean energy $\overline{E}$ and momentum M. A minimum of $\overline{V}$, subject to constraints on $\overline{E}$ and M, will occur at a stationary point of the function

$$F(y_1, y_2, y_3; Q_i(y)) = \overline{V} + \lambda\overline{E} + \mu M,$$

where λ and μ are Lagrange multipliers. The equations for the stationary points of F result in five equations in the five unknowns $\{y_1, y_2, y_3, \lambda, \mu\}$, namely

$$\frac{\partial F}{\partial y_1} = \frac{\partial F}{\partial y_2} = \frac{\partial F}{\partial y_3} = 0, \quad \overline{E} = E_0, \quad M = M_0. \tag{3.4}$$

The partial derivatives of F can be evaluated from

$$\begin{aligned}
\frac{\partial F}{\partial y_1} &= (Q_m - Q_1(y_1)), (-(\phi(y_1) - \phi_m) + 2\lambda(\psi_1(y_1) - \psi_m) + \mu(y_2 - y_1)),\\
\frac{\partial F}{\partial y_2} &= (Q_m - Q_1(y_2))((\phi(y_2) - \phi_m) - 2\lambda(\psi_1(y_2) - \psi_m) + \mu(y_2 - y_1)),\\
\frac{\partial F}{\partial y_3} &= Q_2(y_3)(\phi(y_3) + 2\lambda\psi_2(y_3) - 2\mu y_3),
\end{aligned}$$

where ϕ is defined by

$$\phi_{yy} - \phi = (\psi_1 - \psi_2), \quad \phi_y = 0, \quad \text{on} \quad y = \pm\frac{L_y}{2}, \tag{3.5}$$

and

$$\phi_m = \frac{1}{y_2 - y_1} \int_{y_1}^{y_2} \phi\,\mathrm{d}y, \quad \psi_{im} = \frac{1}{y_2 - y_1} \int_{y_1}^{y_2} \psi_i\,\mathrm{d}y, \quad i = 1, 2.$$

The nonlinear system (3.4) is solved using Broyden's method (a multi-dimensional secant method, see Press *et al.* 1996, Chap. 9.7). For all values of $\beta \in [0.2, 0.5]$, $\sigma \in [1.5, 3]$, a single, and apparently unique, solution $\{Y_1, Y_2, Y_3\}$ is found. It is easily verified that a given solution is a (local) minimum of $\overline{V}$, subject to the constraints, by calculating $\overline{V}$ numerically when the solution is slightly perturbed, i.e. at $\{Y_1 + \delta y_1, Y_2 + \delta y_2, Y_3 + \delta y_3\}$. In order that the constraints are accounted for, the perturbations must satisfy

$$\delta y_1 \frac{\partial M}{\partial y_1} + \delta y_2 \frac{\partial M}{\partial y_2} + \delta y_3 \frac{\partial M}{\partial y_3} = \delta y_1 \frac{\partial \overline{E}}{\partial y_1} + \delta y_2 \frac{\partial \overline{E}}{\partial y_2} + \delta y_3 \frac{\partial \overline{E}}{\partial y_3} = 0.$$

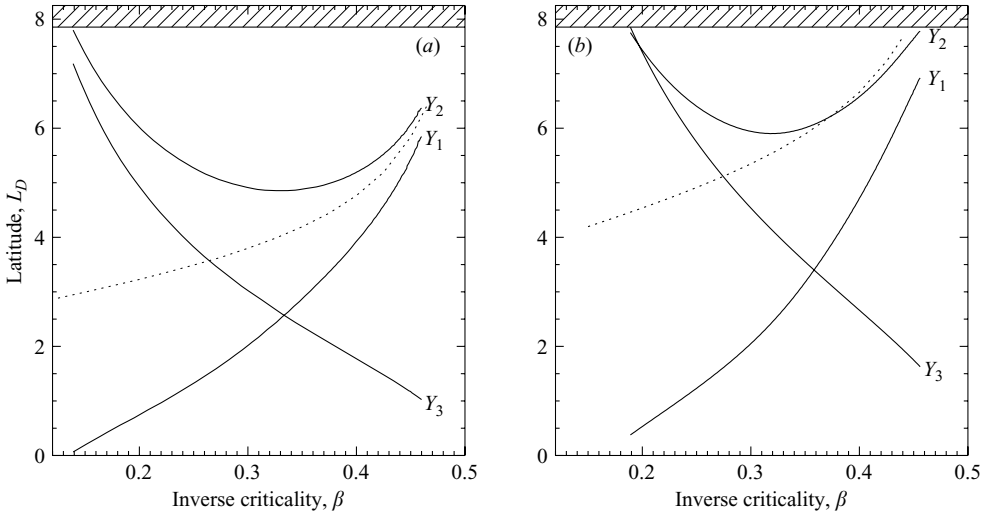

FIGURE 5. The solutions $\{Y_1, Y_2, Y_3\}$ of the nonlinear system defined by (3.4) against β, for two different initial jet widths $\sigma = 2$ (a), $\sigma = 3$ (b). The solutions $\{Y_1, Y_2, Y_3\}$ are the EPVH predictions for the latitudes bounding the mixing regions shown in figure 1(b). The dotted curves show the latitude y_c of the upper-layer critical line of the fastest growing normal mode of the initial flow, calculated as described in the text.

In each case it is found that

$$\overline{V}(Y_1 + \delta y_1, Y_2 + \delta y_2, Y_3 + \delta y_3) > \overline{V}(Y_1, Y_2, Y_3).$$

The EPVH prediction for the final PV field q_i is therefore given by (3.1) with $\{y_1, y_2, y_3\} = \{Y_1, Y_2, Y_3\}$. This q_i is then used to obtain the final streamfunction ψ_i and zonal velocity u_i as described above.

The use of the constraints confers the following desirable property on the solutions $\{Y_1, Y_2, Y_3\}$: as β increases towards the Charney–Stern–Pedlosky stability boundary at $\beta = 0.5$, the predicted mixing regions shrink to zero as $Y_3 \to 0$ and $Y_1 \to Y_2$. For stable flows with $\beta > 0.5$, the system (3.4) has no solutions satisfying $Y_3 > 0$, $Y_2 > Y_1 > 0$. Hence no PV mixing, and therefore no change to the initial jet, is predicted for stable flows. This can be understood because latitudinal PV mixing, such as that illustrated in figure 1(b), cannot occur in a stable flow without changing the total momentum M (see e.g. Shepherd 1988). Figure 5 shows $\{Y_1, Y_2, Y_3\}$ as a function of β for two different values of the initial jet width ($\sigma = 2, 3$). At relatively low values of β, the mixing regions extend right across the channel in the lower layer, and from the centre of the channel to the sidewalls in the upper layer. At higher values of β, PV mixing is predicted to be confined to thin layers at the centre of the lower layer and at the jet flanks in the upper layer.

Nakamura (1999) has emphasized that linear theory, specifically the location of the critical lines of the fastest growing linear mode, can be used to predict the regions where mixing occurs in the upper layer. For comparative purposes, figure 5 also shows the latitudes of the upper-layer critical lines of the fastest growing normal mode evaluated from linear calculations (dotted curves). The fastest growing normal mode is calculated numerically by first linearizing (2.2)–(2.4) about the initial flow state and then seeking solutions of the form

$$\psi_i = \Psi_i(y) \exp\{\mathrm{i}k(x - ct)\}, \quad i = 1, 2.$$

The linear equations for the complex structure functions $\Psi_i(y)\,(\mathrm{i}=1,2)$ are then discretized following Swanson & Pierrehumbert (1994), and the resulting eigenvalue problem for the complex wave speeds $c = c_r + \mathrm{i}c_i$ is solved using a standard linear algebra package (e.g. Press *et al.* 1996). The zonal wavenumber k is varied continuously until the value that yields the maximum growth rate kc_i for the fastest growing normal mode is found. The critical latitude y_c is defined as the latitude where the real phase speed of this mode equals the upper-layer flow speed, i.e. where $U_1(y_c) - c_r = 0$. The above calculations are repeated for different values of β in order to plot y_c in figure 5 (dotted curves). For both jet widths shown ($\sigma = 2, 3$) the critical lines y_c are seen to lie within (or very close to) the mixing region predicted by the EPVH theory ($Y_1 < y < Y_2$). Hence the EPVH theory is broadly consistent with the expectation from linear theory that mixing will develop in the upper-layer in the vicinity of the upper layer critical lines of the fastest growing linear mode. It is notable that in flows in which the emergence of the fastest growing mode is suppressed, due to the imposition of an integer wavenumber symmetry for example, assumptions (*b*) and (*d*) tend to be violated. Hence the fastest growing linear mode clearly has an important role in the efficient conversion of the available potential energy.

It is clear from figure 5 that the EPVH theory predicts its own breakdown for two possible reasons. First, there is the possibility that the solution indicates that either of the mixing regions extends to the channel walls, i.e. $Y_2 \to L_y/2$ or $Y_3 \to L_y/2$. For such flows the theory predicts that the presence of the sidewalls must influence the final state. In the simulations $Y_2, Y_3 \to L_y/2$ is found to coincide with the breakdown of assumption (*b*), i.e. in these flows significant energy remains trapped in the waves at the end of the lifecycle. This result is consistent with weakly nonlinear analysis of the marginally unstable problem with a uniform upper layer flow (Warn & Gauthier 1989). In this problem the sidewalls necessarily limit the amplitude of the growing waves and all of the potential energy that is released remains as eddy energy. Flows in which the upper-layer flow is more uniform (see e.g. Feldstein & Held 1989) might therefore be expected to be influenced by the walls in a similar manner.

The second possibility for the breakdown of the EPVH theory is that $Y_1 \to 0$. In this limit the 'mixing barrier' separating the mixing regions in the upper layer reduces in horizontal extent until its width becomes zero at $Y_1 = 0$. This prediction is of considerable interest for understanding geophysical mixing barriers, because the assumption of no mixing across the jet in the upper layer must surely break down in this limit, which will be considered in more detail elsewhere. Here, however, we concentrate on flows for which neither of these situations is predicted. Curves $Y_1 = 0, 1/2$ and $Y_2 = L_y/2, (L_y - 1)/2$ are labelled on figure 2, and are seen to cross the region of parameter space with $\beta \in [0.15, 0.2]$. Below, therefore, we concentrate on verifying the theory by comparison with numerical simulations for $\beta \geqslant 0.2$.

3.3. *Comparison with numerical results*

In this section a direct comparison is made between the EPVH predictions and the results of the corresponding numerical simulations. In figure 6(*a*) the initial ($t = 0$, dashed curve) and final ($t = 250 f_0^{-1}$, solid curve) zonal mean velocities in the channel are shown from the reference $(\beta, \sigma) = (0.25, 2)$ numerical calculation. To establish that the result of this numerical simulation is independent of the diffusivity parameter κ, results from otherwise identical experiments with $\kappa = 7.5 \times 10^{-4}$ (medium κ) and $\kappa = 3 \times 10^{-3}$ (high κ) are shown. Because simulations at the very small values of κ appropriate to geophysical scenarios are not in practice feasible, the aim is

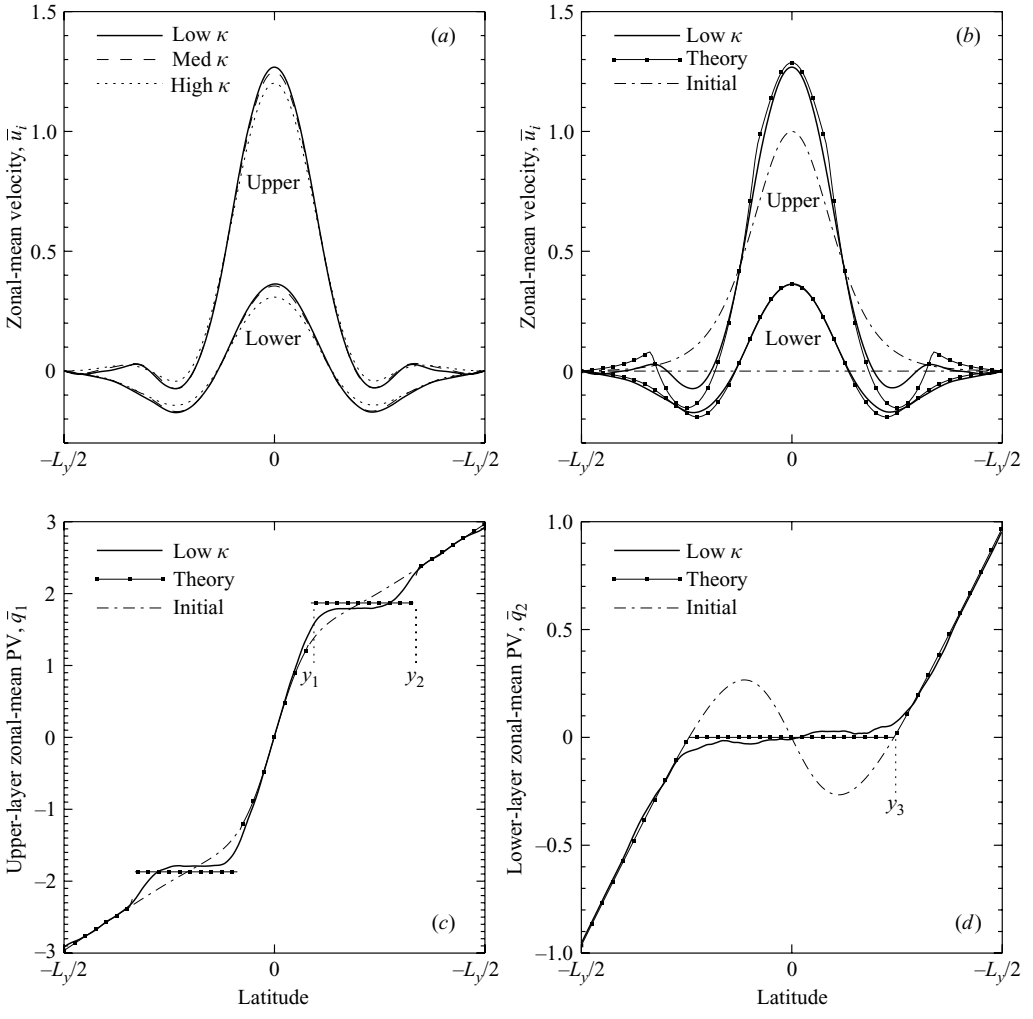

FIGURE 6. (*a*) The zonal mean zonal wind in the upper layer ($\overline{u}_1$) and lower layer ($\overline{u}_2$) at $t = 250 f_0^{-1}$ in the low (2×10^{-4}, solid curves), medium (7.5×10^{-4}, dashed curves) and high (3×10^{-3}, dotted curves) κ reference experiments. (*b*) The zonal mean zonal wind in the upper layer ($\overline{u}_1$) and lower layer ($\overline{u}_2$) at $t = 250 f_0^{-1}$ in the $(\beta, \sigma) = (0.25, 2)$, low-$\kappa$ reference experiment (solid curve) compared with the prediction from the EPVH theory (curve with squares), and the initial jet (dot-dashed). (*c*) As (*b*) but for the zonal-mean upper-layer PV $\overline{q}_1$. (*d*) As (*b*) but for the zonal-mean lower-layer PV $\overline{q}_2$.

to demonstrate convergence in the simulations as κ decreases. Figure 6(*a*) clearly shows convergence of the zonal mean velocity at the final time ($t = 250 f_0^{-1}$), as is evident in the small difference between the medium- and low-κ jets. The high-κ jet is slightly weaker, consistent with the evolution of the energetics during the simulations (figure 4), as significant total energy is lost to diffusive effects during the high-κ simulation. Nevertheless PV snapshots for the higher-κ simulations (not shown) are found to have identical large-scale qualitative features to those in figure 3. In all simulations, by the final time ($t = 250 f_0^{-1}$), further changes to the jet are negligible, because the energetics cycle described in connection with figure 4 is by then complete.

Figure 6(*b–d*) shows a direct comparison between the results of the EPVH predictions obtained from (3.4) and results from the reference numerical simulation with low κ. In figure 6(*b*) the dashed curve shows the initial jet U_1 (and $U_2 = 0$), the solid curve the final zonal mean jet in each layer ($\overline{u}_1$ and $\overline{u}_2$) from the simulation, and the curve with squares the theoretical prediction for the final jet. It is clear that the theory captures both the horizontal structure and the magnitude of the final jet in each layer. The only region in which there is not excellent agreement between the EPVH theory and the simulated jet is in the weak negative (westward) jets to the flanks of the main jet in the upper layer. The theory overestimates the strength of these westward jets for reasons that will be discussed below. To help understand the success of the theory in predicting the equilibrated jets, figure 6(*c*, *d*) shows the corresponding zonal mean PV profiles $\overline{q}_1$ and $\overline{q}_2$. From these profiles it is clear that the EPVH theory has succeeded in correctly predicting the latitudes Y_1, Y_2 and Y_3 that define the regions where PV homogenization takes place, as illustrated in figure 1(*b*). The significance of these latitudes is also clear from the snapshot of the numerical simulation at late times (see figure 3*c*, *d*).

Is the agreement as good between the EPVH theory and the remaining simulations? First, predictions for latitudinal temperature fluxes are considered, as this is arguably the most important aspect of the problem from a climate perspective. In the two-layer model, the interfacial height, which is proportional to $(\psi_2 - \psi_1)$ (Pedlosky 1987), serves as a proxy for temperature. To assess the latitudinal transport of temperature (mass) we consider the first latitudinal moment of the interface height

$$\mathscr{H} = \int_D y(\psi_2 - \psi_1)\,\mathrm{d}^2\boldsymbol{x}.$$

The change in $\mathscr{H}$ during the simulations, $\delta\mathscr{H}$, is a measure of the total latitudinal 'heat flux' induced by the eddies. Does the theory accurately predict this quantity at all parameter values? From (2.2), (2.6) and (3.2) it is straightforward to show that the EPVH prediction for $\delta\mathscr{H}$ is

$$\delta\mathscr{H} = \int_D y((q_1 - q_2) - (Q_1 - Q_2))\,\mathrm{d}^2\boldsymbol{x} = 2L_x \int_{-Y_3}^{Y_3} y Q_2\,\mathrm{d}y, \tag{3.6}$$

Figure 7 shows $-\delta\mathscr{H}$ calculated from the simulations plotted against the EPVH prediction (3.6). It is clear that the EPVH theory is successful in predicting this quantity for all of the numerical simulations. However, the prediction for $\delta\mathscr{H}$ is obtained from the initial PV distribution in the lower layer only, and therefore does not constitute a complete test of the theory.

A more complete test is to predict the maximum strength of the final jet in each layer. Figure 8(*a*, *b*) shows the numerical results plotted against the EPVH theoretical predictions for the maximum jet strength in the upper layer, $\mathrm{Max}\{\overline{u}_1\}$, and lower layer, $\mathrm{Max}\{\overline{u}_2\}$. The theory is very successful for the lower-layer jet, and is also successful for the upper layer, except for those simulations with the lowest values of β ($= 0.2$ and 0.225).

Some examples of the different jet shapes to emerge are shown in figure 8(*c*, *d*), where initial, theoretical and modelled jets are plotted. For $(\beta, \sigma) = (0.3, 3)$ the initial jet is broad and the initial instability is relatively weak. The corresponding upper-layer mixing regions are far from the flanks of the jet, and a broad 'bulbous' jet emerges, the shape and strength of which is predicted by the theory except in the regions of westward flow. For $(\beta, \sigma) = (0.2, 1.5)$, by contrast, the initial jet is narrow and the

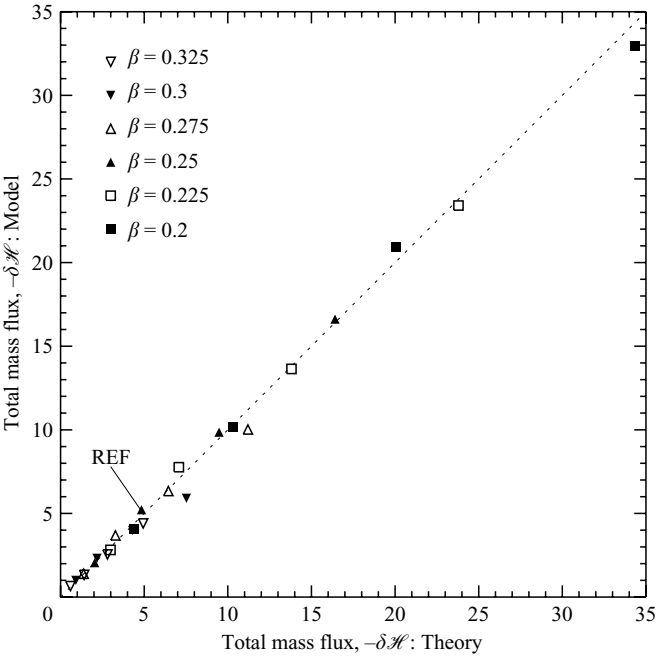

FIGURE 7. EPVH theoretical predictions for the total latitudinal mass flux $-\delta\mathscr{H}$ against $-\delta\mathscr{H}$ calculated from the numerical experiments at $t = 250 f_0^{-1}$.

resulting upper-layer mixing regions extend near to the jet centre. As a result, the final jet has a triangular shape, and its exact magnitude is not predicted accurately by the theory, although its total eastward momentum (not shown) is accurately estimated. Examination of the EPVH predicted state reveals a thin region of strong PV gradient at the jet core in the upper layer between latitudes $-Y_1$ and Y_1. In the simulation this region is too thin ($\lesssim L_D$) to maintain its integrity during the turbulent evolution of the flow, and a combination of weak mixing across it, and the presence of small-amplitude waves, prevent the predicted state from being realized exactly in the zonal mean. This explains why the theory is less accurate for the upper layer jet in cases where $Y_1 \lesssim 1$ (i.e. for $\beta = 0.2$ and 0.225). For similar reasons the predicted sharp jumps in PV at the edges of the upper-layer mixing regions (i.e. at $\pm Y_1$, $\pm Y_2$) are smoothed considerably in the simulations. Instead, the change in zonal mean PV occurs across a distance of approximately L_D, as is seen in figure 6(*c*). It is the difference in sharpness of these PV jumps that accounts for the differences in amplitude of the weak westward jets, located at the flanks of the main upper-layer jet, between the predicted states and the simulations.

4. A statistical mechanics approach

A statistical mechanics approach to the baroclinic lifecycle problem can also be formulated (Miller 1990; Robert 1991; Robert & Sommeria 1991). Below, we compare the predictions made by a statistical mechanics theory to those of the EPVH theory above. The Miller–Robert 'maximum-entropy' approach aims to predict the final state by defining and maximizing a mixing entropy under suitable conditions. It has been described as an 'Empirical statistical theory with many constraints' (ESTMC) (see the recent review of Majda & Wang 2006).

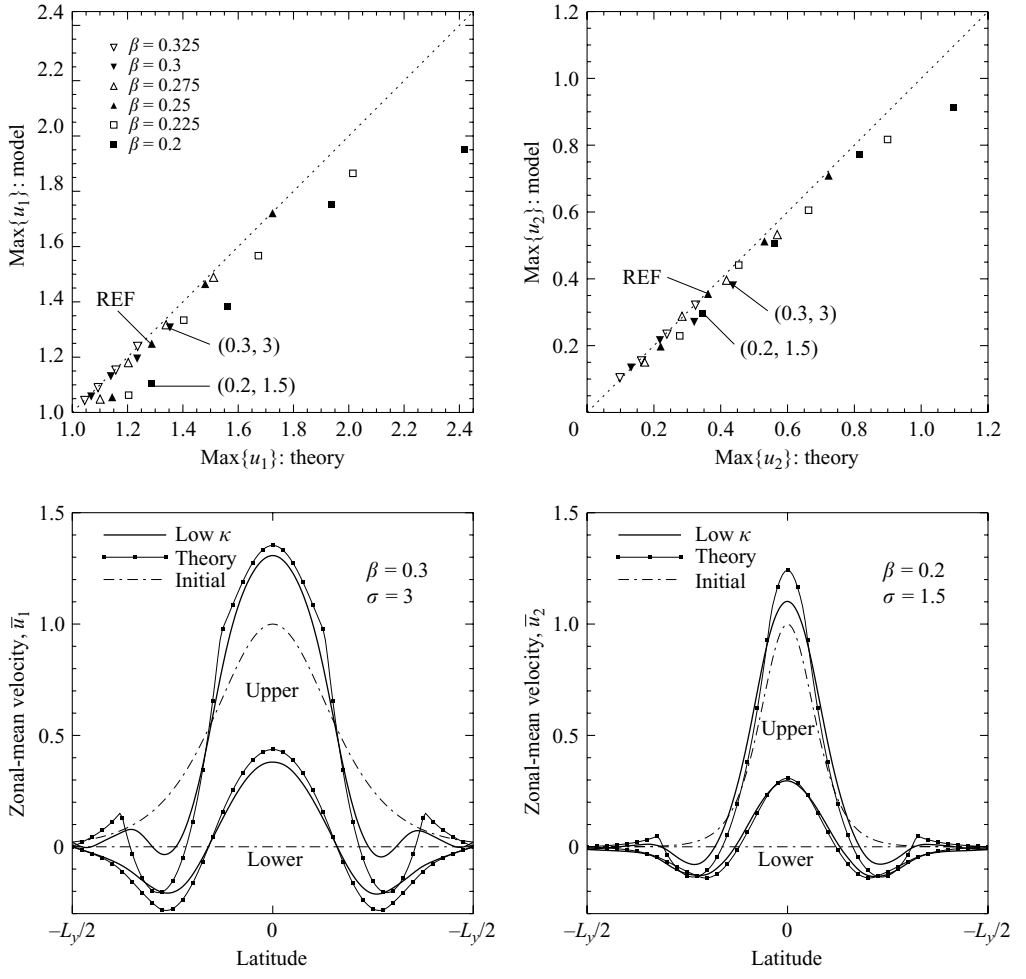

FIGURE 8. (*a*) The maximum value of the final upper-layer zonal-mean wind $\overline{u}_1$ as predicted from the EPVH theory against that calculated from the numerical experiments at $t = 250 f_0^{-1}$. (*b*) As (*a*) but for the lower-layer zonal-mean wind $\overline{u}_2$. (*c*) Direct comparison between EPVH and calculated $\overline{u}_1$, $\overline{u}_2$ for the $(\beta, \sigma) = (0.3, 3)$ simulation. (*d*) As (*c*) but for the $(\beta, \sigma) = (0.2, 1.5)$ simulation.

The localized nature of the PV mixing observed in figure 3 suggests that ergodicity, the assumption of which is implicit to the ESTMC theory, may not be attained in practice in the simulations. Non-attainment of ergodicity has been previously cited as a reason for the failure of ESTMC statistical predictions for flows in which large-scale (potential) vorticity gradients are present (Chavanis & Sommeria 1998; Brands *et al.* 1999; Prieto & Schubert 2001). Various empirical improvements to the theory, such as restricting mixing-entropy maximization to part of the domain, have been proposed. However, for the current problem it far from obvious *a priori* which restrictions of this type should be used. Hence we proceed below with a comparison with the unrestricted ESTMC theory as commonly applied.

Otherwise, the ESTMC theory is well suited for comparison with the EPVH predictions described above, as all possible Casimir constraints (2.8), together with the momentum and energy constraints (2.6) and (2.7) are naturally incorporated as part of

the theory. In ESTMC theory, the Casimir invariants are enforced simultaneously by constraining the equilibrated PV, $q_i \in \mathscr{R}(Q_i)$, i.e. to be obtainable via a conservative rearrangement of the initial PV field in each layer. This constraint is imposed by expressing the final PV field $q_i(y)$ (or 'macrostate') as a mixture of the initial PV distribution throughout that layer. To describe this mixture, a density function $\rho_i(y, \sigma)$, which describes the proportion of fluid parcels with PV equal to σ at a given latitude y in layer i is introduced. (Note that any coarse-graining or averaging process could act instead of the zonal mean taken here). The density function ρ_i is constrained to satisfy

$$\int \rho_i(y, \sigma)\, \mathrm{d}\sigma = 1, \tag{4.1}$$

and it is related to the zonal mean potential vorticity via

$$\int \sigma \rho_i(y, \sigma)\, \mathrm{d}\sigma = q_i(y) \tag{4.2}$$

The constraints $\{M = M_0, \overline{E} = E_0, q_i \in \mathscr{R}(Q_i),\ i = 1, 2.\}$, formulated in terms of ρ_i respectively become

$$\left.\begin{aligned} M &= L_x \sum_{i=1}^{2} \int_{-L_y/2}^{L_y/2} \int y \sigma \rho_i(y, \sigma)\, \mathrm{d}\sigma\, \mathrm{d}y = M_0, \\ \overline{E} &= -\frac{L_x}{2} \sum_{i=1}^{2} \int_{-L_y/2}^{L_y/2} \int \sigma \psi_i(y)\, \rho_i(y, \sigma)\, \mathrm{d}\sigma\, \mathrm{d}y = E_0, \\ A_i(\sigma) &= \int_{-L_y/2}^{L_y/2} \rho_i(y, \sigma)\, \mathrm{d}y = A_{0i}(\sigma). \end{aligned}\right\} \tag{4.3}$$

Note that the streamfunction ψ_i $(i = 1, 2)$ implicitly depends on both ρ_1 and ρ_2 through (2.2). The function

$$A_{0i}(\sigma) = \sum_{Q_i(y_j) = \sigma} \frac{1}{Q_{iy}(y_j)},$$

represents the initial 'area' occupied by the PV level σ. The set of conservative rearrangements $\mathscr{R}(Q_i)$ is therefore defined by (4.3) and (4.1). Note that this representation is easily modified to allow integrable singularities in the $A_{0i}(\sigma)$ field (i.e. where $Q_{iy}(\sigma) = 0$), or indeed finite regions of constant PV in the initial fields.

Under the assumption that the statistics of the equilibrated flow are independent of x, as observed in the numerical simulations, the introduction of the density function $\rho_i(y, \sigma)$ allows a mixing entropy S to be defined. For a given large-scale equilibrated state $q_i(y)$, or 'macro-state', the mixing entropy

$$S = -\sum_{i=1}^{2} \int \rho_i \log \rho_i\, \mathrm{d}\sigma\, \mathrm{d}y \tag{4.4}$$

can be considered to be a measure of the number of possible arrangements, or 'micro-states', of equal-size small-scale vortices that correspond to a given macro-state (4.2). Under the 'ergodic hypothesis' that all micro-states are realizable and have comparable probabilities, maximizing S corresponds to finding the most likely macro-state to emerge. Statistical arguments (Robert 1991; Robert & Sommeria 1991) reveal that the vast majority of micro-states are close (in some sense) to this most

probable macro-state, and if the ergodic hypothesis holds the most probable macro-state will therefore be a good prediction for the equilibrated state. For a relatively straightforward summary of the Miller–Robert argument in the geophysical context see e.g. Prieto & Schubert (2001) or Majda & Wang (2006, Chap. 9).

In order to maximize S under the constraints (2.6)–(2.8), the extremals of the functional

$$\mathscr{F} = S + \lambda\overline{E} + \mu M + \sum_{i=1}^{2} \alpha_i(\sigma) A_i(\sigma),$$

are sought, where λ, μ and $\alpha_i(\sigma)$ are Lagrange multipliers. Taking the first variation results in

$$\int\int \sum_{i=1}^{2} \delta\rho_i(-\log\rho_i - 1 + \sigma(\lambda\psi_i + \mu y) + \alpha_i(\sigma))\,\mathrm{d}\sigma\,\mathrm{d}y = 0.$$

The above must hold for any admissible variation $\delta\rho_i$ $(i = 1, 2)$, hence it follows that

$$\rho_i(y,\sigma) = \frac{1}{Z_i(y)} \exp\{\sigma(\lambda\psi_i + \mu y) + \alpha_i(\sigma)\}, \tag{4.5}$$

where

$$Z_i(y) = \int \exp\{\sigma(\lambda\psi_i + \mu y) + \alpha_i(\sigma)\}\,\mathrm{d}\sigma$$

is a partition function introduced in order to satisfy the remaining constraint (4.1).

For a given $Q_i(y)$, M_0 and E_0, the system (4.5) together with constraints (2.6)–(2.8) can be discretized on a grid of N points to form a system of $2N + 2$ nonlinear equations, which can be solved numerically using standard methods as described in the Appendix. Following previous studies of this type (e.g. Prieto & Schubert 2001), we assume that solutions of of (4.5) uniquely maximize the functional $\mathscr{F}$. Some discussion of the formal conditions under which this assumption is valid is given in Robert & Sommeria (1991). That the particular state found *locally* maximizes the mixing entropy S is verified numerically in § 5 below.

Figure 9 (dotted curve) shows quantities derived from the maximum-entropy state calculated for the reference $(\beta, \sigma) = (0.25, 2)$ case described above, along with the same quantities calculated from the EPVH theory (curves with squares), and the results from the low-κ numerical experiment (solid curves, see also figure 6). The four panels show latitudinal profiles of upper- and lower-layer zonal mean velocities $\overline{u}_1$, $\overline{u}_2$ and zonal mean PV fields $\overline{q}_1$, $\overline{q}_2$. The results are typical of the maximum-entropy states found for all of the two-layer flows investigated. The upper-layer jet is of approximately the correct strength, but is broader than that seen in the simulations, and the regions of westward flow at the flanks of the jet are too broad and strong. The lower-layer jet is both too strong and too broad. The upper-layer PV field does not differ greatly from the initial state (shown in figure 6); in particular there is no PV homogenization at the jet flanks. The lower-layer PV field has a strong positive gradient in the centre of the channel compared to the near zero gradient seen in the simulations. In summary, the maximum entropy theory is markedly less successful in describing the simulated final flow than the EPVH theory (solid curve with squares). The limited success that the maximum-entropy theory does enjoy is arguably due to the restrictions imposed on the final state by the constraints, as opposed to any noticeable tendency towards mixing-entropy maximization in the simulations. The final state predicted for the lower layer PV field (figure 9*d*) is in particular very

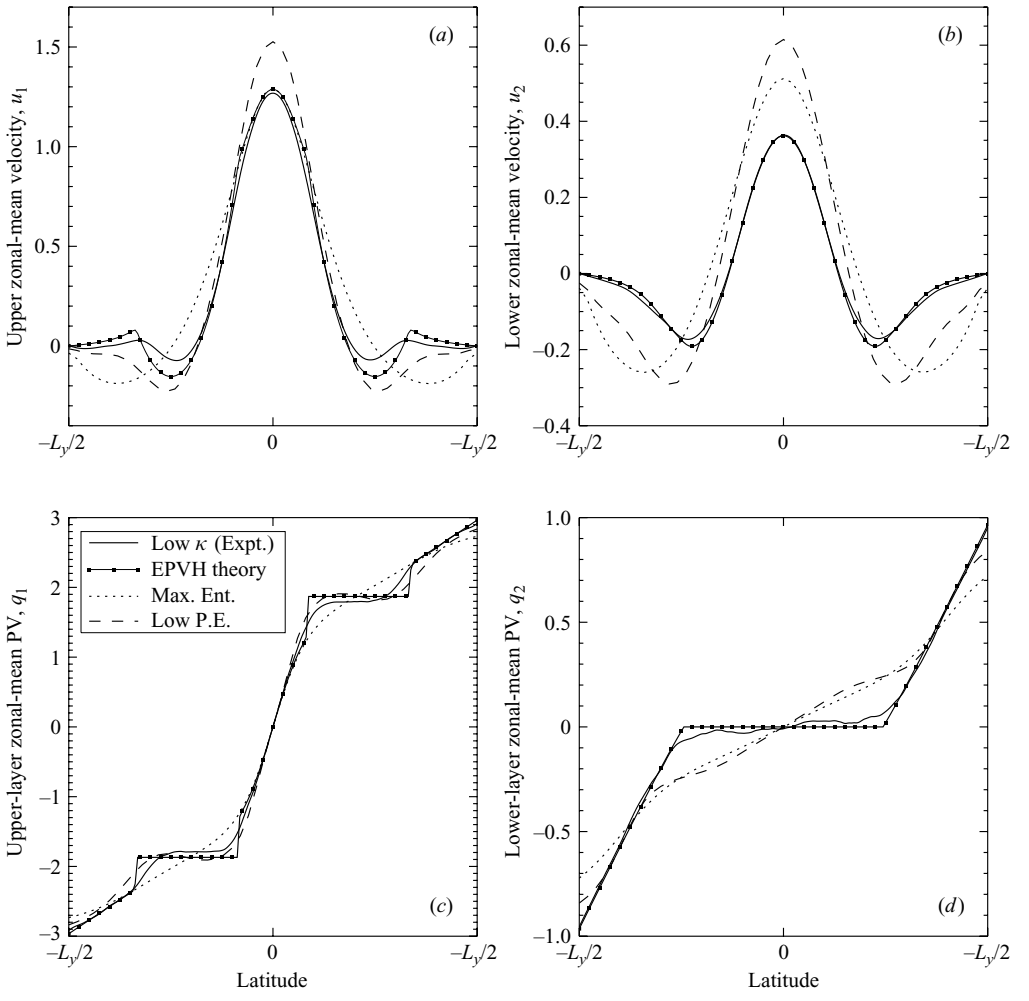

FIGURE 9. (*a*) Upper-layer zonal-mean zonal wind $\overline{u}_1$ at $t = 250 f_0^{-1}$ in the low-κ reference experiment $(\beta, \sigma) = (0.25, 2)$ (solid curve), $\overline{u}_1$ predicted by the EPVH theory (curve with squares), $\overline{u}_1$ predicted by the maximum entropy theory (dotted curve) and $\overline{u}_1$ in the low-potential-energy state, corresponding to $\nu = -40$, calculated as described in the text (dashed curve). (*b–d*) As (*a*) but for (*b*) lower-layer zonal-mean wind $\overline{u}_2$, (*c*) upper-layer zonal-mean PV $\overline{q}_1$, (*d*) lower-layer zonal-mean PV $\overline{q}_2$.

different from that seen in the simulations. For the maximum-entropy state to be attained, bands of fluid would need to be 'exchanged' in latitude in the lower layer, with only limited mixing between them. Such an exchange flow in the lower layer is not observed in any of the simulations.

5. Low-potential-energy states and exploration of the solution manifold

In this section the maximum-entropy theory approach is adapted in order to explore other possible 'equilibrated' states satisfying the known dynamical constraints associated with the initial flow (2.6)–(2.8), $\{M = M_0, \overline{E} = E_0, q_i \in \mathscr{R}(Q_i),\ i = 1, 2.\}$. Ideally, we would like to determine the absolute minimum-potential-energy state

satisfying the dynamical constraints, in order to assess the importance of the additional kinematic constraint of PV homogenization used in the EPVH theory of § 3.

In principle, the minimum potential energy could be obtained by finding the extremal functions of the functional

$$\mathscr{G}^* = \overline{V} + \lambda^* \overline{E} + \mu^* M + \sum_{i=1}^{2} \alpha_i^*(\sigma) A_i(\sigma), \tag{5.1}$$

where λ^*, μ^*, $\alpha_i^*(\sigma)$ are Lagrange multipliers as above. However, technical difficulties arise in the direct calculation of the extremal functions of $\mathscr{G}^*$. In order to proceed, therefore, the problem is regularized by including the mixing entropy as follows:

$$\mathscr{G}^* = \lim_{\nu^* \to 0} \overline{V} + \lambda^* \overline{E} + \mu^* M + \sum_{i=1}^{2} \alpha_i^*(\sigma) A_i(\sigma) + \nu^* S. \tag{5.2}$$

This formulation allows the maximum-entropy methodology described above to be exploited. In practice calculations must be made at finite values of ν^*, allowing the limit $\nu^* \to 0$ to be examined numerically. It turns out that numerical convergence in this limit is elusive, as increasingly small horizontal scales develop in the calculated state as $|\nu^*|$ is decreased, and progressively higher numerical resolution (higher N) is required. However, the finite ν^* calculations remain of interest, as these are extremals of potential energy $\overline{V}$, subject to the dynamical constraints, *at fixed mixing entropy* S. By finding extremal functions of $\mathscr{G}^*$, states with progressively lower (or higher) potential energy on the solution manifold $\{M = M_0, \overline{E} = E_0, q_i \in \mathscr{R}(Q_i),\ i = 1, 2.\}$ can be found by varying ν^*, which acts as a control parameter.

To make the above calculation explicit, the problem is reformulated (dividing by ν^* and re-labelling the multipliers) to give

$$\mathscr{G} = \lim_{\nu \to \pm\infty} S + \nu \overline{V} + \lambda \overline{E} + \mu M + \sum_{i=1}^{2} \alpha_i(\sigma) A_i(\sigma). \tag{5.3}$$

At finite ν the functional $\mathscr{G}$ can be treated exactly as $\mathscr{F}$ above, and the numerical method described in the Appendix can be used to calculate ρ_i from the nonlinear system defined by

$$\rho_i(y, \sigma) = \frac{1}{Z_i(y)} \exp\{\sigma(\nu\phi + \lambda\psi_i + \mu y) + \alpha_i(\sigma)\}, \tag{5.4}$$

where

$$Z_i(y) = \int \exp\{\sigma(\nu\phi + \lambda\psi_i + \mu y) + \alpha_i(\sigma)\}\, \mathrm{d}\sigma,$$

together with the constraints. Setting $\nu = 0$ recovers the maximum-mixing-entropy state described above. Values of $\nu > 0$ result in progressively higher-potential-energy states, and $\nu < 0$ results in progressively lower-potential-energy states. Figure 10 shows the mixing entropy S and potential energy $\overline{V}$ of the explicitly calculated states obtained in the range $\nu \in [-40, 5]$. Converged solutions with lower potential energy ($\nu < -40$) have also been calculated, but as discussed above develop progressively smaller-scale structure in $q_i(y)$, which first appears in the jet flanks in the upper layer. Also shown in figure 10 are the initial potential energy V_0, the EPVH theory prediction, and the final ($t = 250 f_0^{-1}$) potential energy in the low-κ numerical experiment. Figure 10 lends numerical support to the idea that the maximum-entropy state calculated in § 4 is indeed a (local) maximum of the mixing entropy S. Several test functions have been

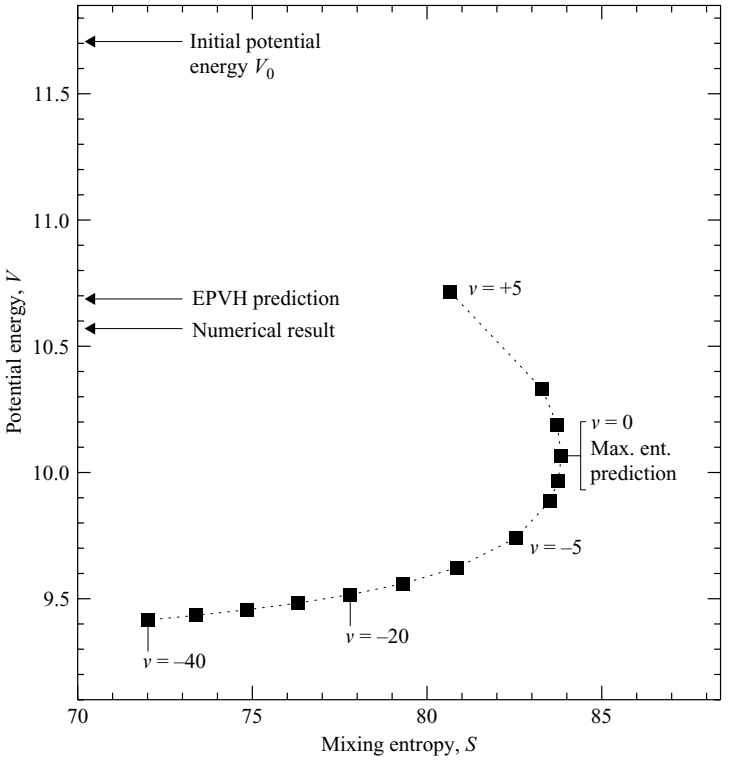

FIGURE 10. Location of calculated states, derived from the reference problem $(\beta, \sigma) = (0.25, 2)$, as a function of mixing entropy S and potential energy V. Note that mixing entropy is defined only up to the addition of an arbitrary constant. The maximum entropy state corresponds to $\nu = 0$. The potential energy in the initial state V_0 is shown, as is the potential energy in the state predicted by the EPVH theory, and that in the numerical calculation.

used in place of ϕ in (5.4), in order to verify that $\nu = 0$ corresponds to a maximum of S in each case.

The $\nu = -40$ solution is plotted in figure 9 (dashed curve) as an example of a low-potential-energy state satisfying the dynamical constraints. The upper- and lower-layer jets are seen to be much stronger than those of the numerical simulations, the lower-layer PV resembles that seen in the maximum entropy state, and the upper-layer PV resembles that in the simulations; PV mixing has occurred in the jet flanks. Efficient release of available potential energy can therefore be associated with both mixing in the upper-layer jet flanks, which is observed in the simulations, and an exchange flow in the lower layer, which is not.

A useful concept is the efficiency $\mathscr{E}$ of potential energy release, defined as the ratio of available potential energy released in the simulations to that calculated to be available from the initial flow, considering all known dynamical constraints. Figure 10 shows explicitly that $\mathscr{E} \lesssim 50\%$ in the reference simulation. This result is significant as it highlights the importance of the additional kinematic constraint of PV homogenization in the EPVH theory. In the final state predicted by the EPVH theory, the potential energy cannot be reduced further (as the predicted state is stable according to the Charney–Stern–Pedlosky criterion), but, with respect to the initial state, potential energy has been released 'inefficiently' because the global minimum of V associated with the initial conditions is far from being attained. Any theory of

atmospheric or oceanic eddy heat transport must therefore (implicitly or explicitly) take account of this inefficiency in potential energy release.

6. Conclusions

Previous theories of the 'adjustment' of unstable baroclinic jets have focused on predicting eddy-driven changes to the mean flow that act to stabilize the jet to linear normal mode disturbances (e.g. Stone 1978). The problem with such theories is that there are infinitely many ways such stabilization can be achieved. In their simplest formulations, the adjustment approaches do not address the question of why upgradient momentum fluxes develop in such flows, leading to an overall acceleration of the jet (e.g. Simmons & Hoskins 1978; James 1987). Although attempts have been made to modify baroclinic adjustment theories to consider upgradient momentum fluxes (notably by Nakamura 1993, 1999), the resulting theories have been heuristic in nature and have not made definite predictions. Here a theory has been developed, 'equilibration via potential vorticity homogenization' (EPVH), that makes a definite prediction for a final equilibrated jet. The EPVH theory accounts for the upgradient momentum fluxes, the total latitudinal heat fluxes, and the shape of the final jet, as observed across a range of parameter settings in quasi-geostrophic two-layer numerical simulations. Interestingly, for the simple formulation presented here, the EPVH theory also predicts its own breakdown for a number of reasons described above.

The success of the EPVH theory is in part due to the correct treatment of the dynamical constraints on the flows under consideration, particularly the constraints on the total momentum and energy. However, the alternative theories explored in § 4 (the 'ESTMC' maximum entropy theory of Miller 1990; Robert 1991), and § 5 (where a low-potential-energy state was calculated) were subject to the same constraints, and were significantly less successful (see figure 9). Two further ingredients are important in the EPVH theory: the assumption of PV homogenization within well-delineated regions, and the minimization of available potential energy.

The first of these, the PV homogenization assumption, is supported empirically by direct observations and numerical simulations of a wide range of geophysical flows (e.g. Rhines 1975, 1994; Dritschel & McIntyre 2008). That PV homogenization occurs in well-delineated regions can be argued to be a phenomenological consequence of 'Rossby wave elasticity' (e.g. McIntyre 1994). In regions where PV gradients are strong, Rossby wave-like motions persist, whereas where they are weak PV gradients can easily be overcome, initiating turbulence and mixing which then proceeds to completion. That PV mixing proceeds in this fashion can be regarded as a kinematic constraint on the development of the flow.

The minimization of available potential energy is, by definition, a requirement that the instability proceeds to completion, i.e. it acts to stabilize the final state to any further permissible disturbances. The role of the kinematic constraint of PV homogenization in determining the minimum-potential-energy state can be seen by comparing the calculated flow, the EPVH prediction and the low-potential-energy state calculated in § 5 (for which the kinematic constraint is not imposed). The kinematic constraint is seen to have the effect of reducing the 'efficiency' $\mathscr{E}$ of potential energy released to below 50% of that available in its absence. This result highlights the necessity of accounting for the strong tendency towards PV homogenization in any predictive theory of quasi-two-dimensional turbulence on the β-plane.

The relative failure of both the ESTMC theory and the low-potential-energy calculation is associated with each predicting an 'exchange flow' in the lower layer of the channel. Such a flow, in which bands of fluid exchange position with only relatively weak mixing taking place between them, is theoretically possible under the dynamical constraints but is not observed in the simulations. For the maximum entropy (ESTMC) theory, one explanation is the non-applicability of the 'ergodic hypothesis' at the final time in the simulation; it might be argued that if a truly inviscid simulation were integrated for a longer time then the ESTMC state might begin to emerge. However, there is no hint of this in the simulations. It might also be argued that the ESTMC theory is not applicable to the baroclinic flow investigated here, since it is governed by a distinct energetics cycle (figure 4), unlike other idealized two-dimensional turbulent situations (e.g. those considered by Sommeria, Staquet & Robert 1991).

The main challenge in the further development of the EPVH theory is to apply it to forced–dissipative baroclinic turbulence. Can the 'climates' of model simulations be accurately predicted using a similar approach to that taken here? Thompson & Young (2007) have recently shown that careful account must be taken of the magnitude and form of the forcing and dissipation in any such predictions, an aspect that previous turbulent scaling theories (e.g. Held & Larichev 1996) have often neglected. Account must be taken of the constraints, which are obviously somewhat different in the forced–dissipative problem (e.g. 'energy balance'). Vallis (1988) also points out that complete PV homogenization is often not attained in forced–dissipative flows. It may therefore be necessary to replace the regions in which complete PV homogenization occurs with regions in which PV is homogenized on a time scale related to the eddy amplitude. Determining whether or not these difficulties can be overcome will be the subject of future work.

J. G. E. acknowledges support from the Nuffield foundation. The three anonymous referees are also thanked for their helpful comments.

Appendix. Numerical methods used to find maximum-entropy and low-potential-energy states

To find a given maximum-entropy state, as defined by (4.5) together with initial energy E_0, momentum M_0, and area functions $A_{i0}(\sigma)$ $(i = 1, 2)$, it is necessary to determine the corresponding values of the Lagrange multipliers $\{\lambda, \nu, \alpha_i(\sigma)\}$. An algorithm to solve this type of problem has been proposed by Turkington & Whitaker (1996, the TW algorithm). The TW algorithm has the extremely important property of global convergence (i.e. a solution of the resulting system of equations can be found from any starting point), but was found to be slow for the purposes of exploring the solution manifold and finding the low-potential-energy states as described above.

In view of the above considerations, a description of a fast, although somewhat less robust, algorithm to discretize and solve the problem defined by (4.5) and the constraints (4.3) follows. Following TW the density function $\rho_i(y, \sigma)$ is replaced by a discrete probability distribution

$$p_{mn,i}, = \frac{1}{Z_{n,i}} \exp\{\sigma_{m,i}(\nu\phi_n + \lambda\psi_{n,i} + \mu y_n) + \alpha_{m,i}\},$$
$$1 \leqslant m \leqslant N^*, \quad 1 \leqslant n \leqslant N, \quad i = 1, 2,$$

where

$$Z_{n,i} = \sum_{m=1}^{N^*} \exp\left\{\sigma_{m,i}(\nu\phi_n + \lambda\psi_{n,i} + \mu y_n) + \alpha_{m,i}\right\}(\delta\sigma)_i.$$

Here N^* is the number of discrete vorticity levels $\sigma_{m,i}$ in each layer and N is the number of discrete latitude bands y_n across the channel, each of width δy. The uniform interval between successive PV levels in each layer is given by $(\delta\sigma)_i$, and $\alpha_{m,i}$ are a set of N^* Lagrange multipliers the values of which are to be determined. The expressions $\psi_{n,i}$ and ϕ_n are discretized solutions of (2.2) and (3.5) respectively, and therefore depend on the discretized PV distribution $q_{n,i}$. Note that under this discretization, the mixing entropy (4.4) and its discretized counterpart are equivalent only up to an additive constant, which is inconsequential.

The algorithm solves simultaneously for the unknown Lagrange multipliers and the corresponding unknown PV distribution $q_{n,i}$. Choosing N^*, N odd and making an assumption of jet symmetry about $y = 0$, the above discretized expressions allow a nonlinear system of $N^* + N + 2$ equations to be formulated, which can be written as

$$\boldsymbol{F}(\boldsymbol{x}) = \boldsymbol{0},$$

where the input vector $\boldsymbol{x}$ contains the $N^* + N + 2$ unknowns

$$\boldsymbol{x}^T = \{\lambda, \mu, \alpha_{m,i}, q_{n,i}\}, \quad 1 \leqslant m \leqslant \frac{N^*+1}{2}, \quad 1 \leqslant n \leqslant \frac{N-1}{2}, \quad i = 1, 2.$$

(If the symmetry condition were relaxed then $2(N^* + N) + 2$ equations would be required.) The vector of nonlinear equations $\boldsymbol{F} = \boldsymbol{0}$ is then

$$\sum_{i=1}^{2}\sum_{m=1}^{N^*}\sum_{n=1}^{N} y_n \sigma_{m,i}\, p_{mn,i}\ \delta y - M_0 = 0, \tag{A 1a}$$

$$\sum_{i=1}^{2}\sum_{m=1}^{N^*}\sum_{n=1}^{N} \psi_{n,i}\sigma_{m,i}\, p_{mn,i}\ \delta y - E_0 = 0, \tag{A 1b}$$

$$\sum_{n=1}^{N} p_{mn,i}\ \delta y - A_{0\,m,i} = 0, \tag{A 1c}$$

$$\sum_{m=1}^{N^*} \sigma_{m,i}\, p_{mn,i} - q_{n,i} = 0, \tag{A 1d}$$

where $p_{mn,i}$ is calculated as a function of the vector $\boldsymbol{x}$.

The utility of the above algorithm derives from the reduction of the problem to a single standard nonlinear system for which standard techniques, such as Broyden's method (Press *et al.* 1996, Chap. 9.7) can be applied, as well as in the fact that it is relatively straightforward to implement. By contrast the TW algorithm consists of an iteration of a nonlinear system that must itself be solved by a damped Newton's method. In practice the system (A1*a–d*) requires a good initial guess in order to obtain convergence. It is ideally suited, however, to problems for which new solutions can be obtained from known solutions (which might be obtained using the TW algorithm, for example) by variation of a parameter, e.g. ν in the calculations of § 5 above.

For the solutions presented in §§4 and 5 above, solutions with $N^* = N = 51$ have been compared with $N^* = N = 101$ and $N^* = N = 151$ and numerical convergence established in each case.

REFERENCES

Arbic, B. K. & Flierl, G. R. 2004 Baroclinically unstable geostrophic turbulence in the limits of strong and weak bottom ekman friction: Application to midocean eddies. *J. Phys. Oceanogr.* **64**, 2257–2273.

Brands, H., Chavanis, P. H., Pasmanter, R. & Sommeria, J. 1999 Maximum entropy versus minimum enstrophy vortices. *Phys. Fluids* **11**, 3465–3477.

Chavanis, P. H. & Sommeria, J. 1998 Classification of robust isolated vortices in two-dimensional hydrodynamics. *J. Fluid Mech.* **356**, 259–296.

Dritschel, D. G. & McIntyre, M. E. 2008 Multiple jets as PV staircases: the Phillips effect and the resilience of eddy-transport barriers. *J. Atmos. Sci.* **65** (in press).

Esler, J. G. & Haynes, P. H. 1999 Mechanisms for wave packet formation and maintenance in a quasi-geostrophic two-layer model. *J. Atmos. Sci.* **56**, 2457–2489.

Feldstein, S. B. & Held, I. M. 1989 Barotropic decay of baroclinic waves in a two-layer beta plane model. *J. Atmos. Sci.* **46**, 3416–3430.

Gutowksi, W. J. 1985 Baroclinic adjustment and midlatitude temperature profiles. *J. Atmos. Sci.* **42**, 1733–1745.

Held, I. M. 2005 The gap between simulation and understanding in climate modeling. *Bull. Am. Met. Soc.* **86**, 1069.

Held, I. M. 2007 Progress and problems in large-scale atmospheric dynamics. In *The Global Circulation of the Atmosphere: Phenomena, Theory, Challenges*, chap. 1. Princeton University Press.

Held, I. M. & Larichev, V. 1996 A scaling theory for horizontally homogeneous, baroclinically unstable flow on a beta plane. *J. Atmos. Sci.* **53**, 946–952.

James, I. N. 1987 Suppression of baroclinic instability in horizontally sheared flows. *J. Atmos. Sci.* **44**, 3710–3720.

Lapeyre, G. & Held, I. M. 2003 Diffusivity, kinetic energy dissipation, and closure theories for the poleward eddy heat flux. *J. Atmos. Sci.* **60**, 2907–2916.

Lee, S. & Held, I. M. 1993 Baroclinic wave packets in models and observations. *J. Atmos. Sci.* **50**, 1413–1428.

Majda, A. J. & Wang, X. 2006 *Nonlinear Dynamics and Statistical Theories for Basic Geophysical Flows*. Cambridge University Press.

Mak, M. 2000 Does an unstable baroclinic wave equilibrate/decay baroclinically or barotropically? *J. Atmos. Sci* **57**, 453–463.

McIntyre, M. E. 1994 The quasi-biennial oscillation (QBO): some points about the terrestrial QBO and the possibility of related phenomena in the solar interior. In *The Solar Engine and its Influence on the Terrestrial Atmosphere and Climate* (Vol. 25 NATO ASI Subseries I, Global environmental change), chap. 2, pp. 293–320. Springer.

McIntyre, M. E. & Shepherd, T. G. 1987 An exact local conservation theorem for finite-amplitude disturbances to non-local shear flows, with remarks on Hamiltonian structure and on Arnol'd's stability theorems. *J. Fluid Mech.* **181**, 527–565.

McWilliams, J. C. 2006 *Fundamentals of Geophysical Fluid Dynamics*. Cambridge University Press.

Miller, J. 1990 Statistical mechanics of Euler's equations in two dimensions. *Phys. Rev. Lett.* **65**, 2137–2140.

Nakamura, N. 1993 Momentum flux, flow symmetry, and the nonlinear barotropic governor. *J. Atmos. Sci.* **50**, 2159–2179.

Nakamura, N. 1999 Baroclinic-barotropic adjustments in a meridionally wide domain. *J. Atmos. Sci.* **56**, 2246–2260.

Pavan, V. & Held, I. M. 1996 The diffusive approximation for eddy fluxes in baroclinically unstable jets. *J. Atmos. Sci.* **52**, 1262–1272.

Pedlosky, J. 1987 *Geophysical Fluid Dynamics*. Springer.

Phillips, N. A. 1951 A simple three-dimensional model for the study of large-scale extratropical flow patterns. *J. Met.* **8**, 381–394.

Press, W. H., Teukolsky, S. A., Vetterling, W. T. & Flannery, B. P. 1996 *Numerical Recipes in Fortran 77*, Second edn. Cambridge University Press.

Prieto, R. & Schubert, W. H. 2001 Analytical predictions for zonally symmetric equilibrium states of the stratospheric polar vortex. *J. Atmos. Sci* **58**, 2709–2728.

Rhines, P. 1975 Waves and turbulence on the beta plane. *J. Fluid. Mech.* **69**, 417–443.

Rhines, P. 1994 Jets. *Chaos* **4**, 313–339.

Robert, R. 1991 A maximum-entropy principle for two-dimensional perfect fluid dynamics. *J. Statist Phys.* **65**, 531–553.

Robert, R. & Sommeria, J. 1991 Statistical equilibrium states for two dimensional flows. *J. Fluid Mech.* **229**, 291–310.

Schneider, T. & Walker, C. C. 2006 Self-organisation of atmospheric macroturbulence into critical states of weak nonlinear eddy-eddy interactions. *J. Atmos. Sci.* **63**, 1569–1585.

Shepherd, T. G. 1988 Nonlinear saturation of baroclinic instability. Part I: The two-layer model. *J. Atmos. Sci.* **45**, 2014–2025.

Simmons, A. J. & Hoskins, B. J. 1978 The lifecycles of some nonlinear baroclinic waves. *J. Atmos. Sci.* **35**, 414–432.

Sommeria, J., Staquet, C. & Robert, R. 1991 Final equilibrium state of a two-dimensional shear layer. *J. Fluid Mech.* **233**, 661–689.

Starr, V. P. 1968 *Physics of Negative Viscosity Phenomena.* McGraw-Hill.

Stone, P. H. 1978 Baroclinic adjustment. *J. Atmos. Sci.* **35**, 561–571.

Swanson, K. & Pierrehumbert, R. T. 1994 Nonlinear wave packet evolution on a baroclinically unstable jet. *J. Atmos. Sci.* **51**, 384–396.

Thompson, A. F. & Young, W. R. 2007 Two-layer baroclinic eddy heat fluxes: zonal flows and energy balance. *J. Atmos. Sci.* **63**, 3214–3231.

Thorncroft, C. D., Hoskins, B. J. & McIntyre, M. E. 1993 Two paradigms of baroclinic wave lifecycle behaviour. *Q. J. R. Met. Soc.* **119**, 17–55.

Turkington, B. & Whitaker, N. 1996 Statistical equilibrium computations of coherent structures in turbulent shear layers. *SIAM J. Sci. Comput.* **17**, 1414–1433.

Vallis, G. K. 1988 Numerical studies of eddy transport properties in eddy-resolving and parameterized models. *Q. J. R. Met. Soc.* **114**, 183–208.

Wardle, R. & Marshall, J. 2000 Representation of eddies in primitive equation models by a PV flux. *J. Phys. Oceanogr.* **30**, 2481–2503.

Warn, T. & Gauthier, P. 1989 Potential vorticity mixing by marginally unstable baroclinic disturbances. *Tellus* **41A**, 115–131.

Zurita-Gotor, P. 2007 The relation between baroclinic adjustment and turbulent diffusion in the two layer model. *J. Atmos. Sci.* **64**, 1284–1300.

Zurita-Gotor, P. & Lindzen, R. S. 2007 Theories of baroclinic adjustment and eddy equilibration. In *The Global Circulation of the Atmosphere: Phenomena, Theory, Challenges*, chap. 2. Princeton University Press.